

# **A space beam combiner for long-baseline interferometry**

**Yao Lin, Randall Bartos, Bob Korechoff, Stuart Shaklan**  
Jet Propulsion Laboratory  
California Institute of Technology  
4800 Oak Grove Drive, CA 91109

## **ABSTRACT**

An experimental beam combiner (BC) is being developed to support the space interferometry program at the Jet Propulsion Laboratory. The beam combiner forms the part of an interferometer where star light collected by the siderostats or telescopes is brought together to produce white light fringes, and to provide wavefront tilt information via guiding spots and beam walk information via shear spots. The assembly and alignment of the BC has been completed. The characterization tests were performed under laboratory conditions with an artificial star and optical delay line. Part of each input beam was used to perform star tracking. The white light interference fringes were obtained over the selected wavelength range from 450 nm to 850 nm. A least-square fit process was used to analyze the fringe initial phase, fringe visibilities and shift errors of the optical path difference (OPD) in the delay line using the dispersed white-light fringes at different OPD positions.

**Keywords:** beam combiner, interferometry, metrology, fringe.

## **1. INTRODUCTION**

The beam combiner (BC) has been developed to support space-based optical interferometers at the Jet Propulsion Laboratory<sup>[1-3]</sup>. The BC forms the part of an interferometer where star light collected by the siderostats or telescopes is brought together to produce interference fringes. Therefore, the BC contains all of the optics and detectors for measuring fringe characteristics. An algorithm is described in this paper for determining the phases of the white-light fringes measured in a long-baseline interferometer. The algorithm uses a set of the dispersed white light fringe images at different OPD positions in the optical delay line to solve for the real OPD of each step, fringe phases and fringe visibilities.

There are two types of beam combiners: those that combine the beams at an angle, forming interference fringes across the image as in Young's double slit experiment; and those that combine the beams in parallel and form fringes by changing the optical path of one arm with respect to the other. The BC presented in the paper is of the latter type. The advantages of this architecture are that spectral dispersion can be easily introduced, while the number of detector pixels is reduced. As long as the fringes are observed in dispersed light, the design does not require a fast scanning mechanism for optical phase measurements.

The performance tests in our laboratory used an artificial star which produced two collimated white light input beams to the BC. An optical delay line with a PZT device was used to change the optical path of one of the input beams. Part of the input beams was used as the guiding beams to perform star tracking. Although many phase shift measurement techniques were developed<sup>[4]</sup>, the techniques require equal phase shifts. The least-square fit (LSF) algorithm presented in the paper does not require the equal phase shift critically.

## 2. OPTICAL DESIGN

### 2.1 Artificial star.

The artificial star (AS) is designed to simulate star light collected by the siderostats or telescopes. The AS produces two parallel collimated beams as the input beams to the BC. The optical schematic is shown in Figure 1. A Mag light is used as the source. Its output is coupled into a 5-micron diameter single mode fiber. The output end of the fiber is positioned at the focus of a parabola. After being reflected from the parabola, the beam output from the fiber is well collimated. A non-polarizing beam splitter window (NPBSW) (R/T = 10:90) reflects a small portion of the beam to a position sensitive device (PSD). The PSD is used to track the movement of the fiber end. Part of the transmitted beam is reflected by a non-polarizing beam splitter (NPBS) (R/T = 40:60) to the BC upper input port. The remaining part of the beam is transmitted through the NPBS, then reflected by the delay line mirror to the BC lower input port. These two beams are aligned parallel. The doublet NPBS was made to have a symmetric design so that the reflected and transmitted beams have the same optical path. Each beam passes through a 30-mm diameter input aperture stop which is aligned to the 30-mm input aperture of the BC. The flat mirror is used as the delay line mirror. The mirror is mounted on a stage that can be translated with a PZT along the incident beam direction. Translating the mirror changes the optical path difference (OPD) of the two input beams to the BC.

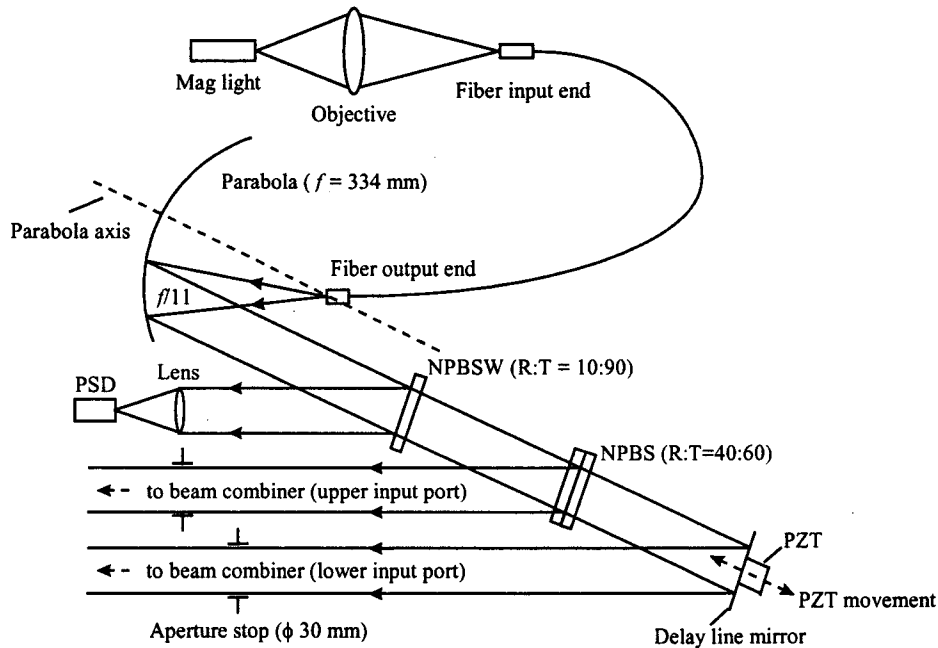
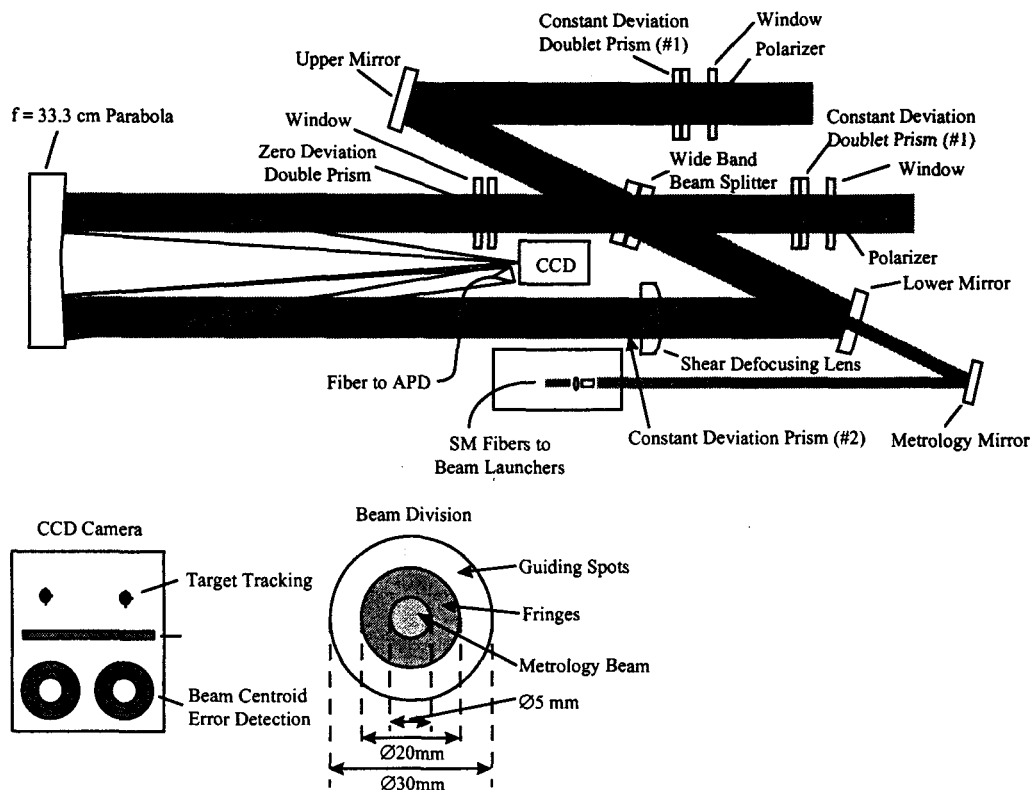


Figure 1. Artificial star.

### 2.2 Beam combiner.

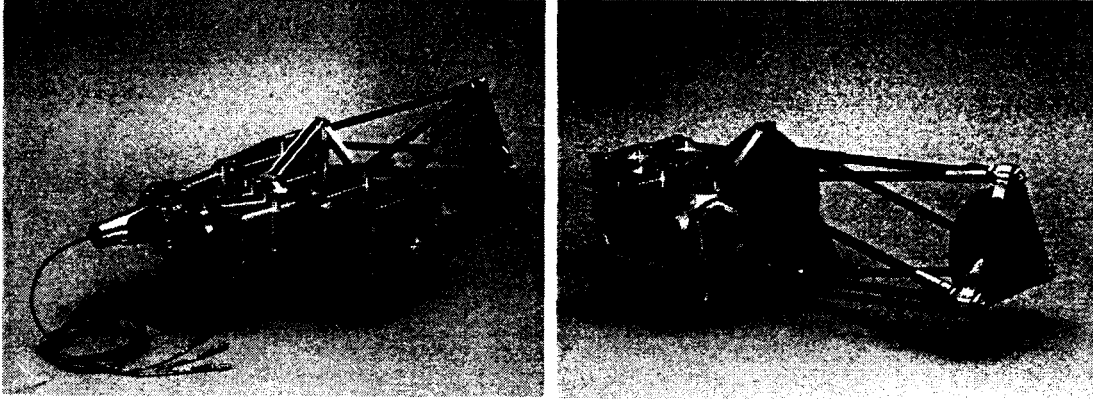
The beam combiner is designed to produce and characterize the white light fringes of two input beams from the same source. The optical schematic is shown in Figure 2. Each input beam is 30-mm diameter, and divided into three parts: the center 5-mm diameter is used for a metrology beam from a beam launcher mounted on the BC; the middle annulus of the beam, from 5 to 20-mm diameter, is used to produce the fringes on a CCD camera; the outer annulus of the beam, from 20 to 30-mm diameter, is used to produce a guiding spot and shear spot on the CCD camera.



**Figure 2.** Optical schematic of the beam combiner.

The middle annuli of the beams from the upper and lower input ports are combined at the doublet wide band beam splitter inside the BC. Part of the combined beam pass through the zero deviation prism where the beam is deviated as a function of wavelength, then is focused by a parabola onto the CCD camera to form dispersed fringes. The doublet zero deviation prism produces zero deviation to the center wavelength of the spectral region of interest. The other part of the combined beam is diverted to the fold (lower) mirror, then reflected to the constant deviation prism (#2). The beam is focused by the parabola onto the avalanche photo diode (APD) to produce a signal to noise ratio of the dispersed fringes. The outer annuluses of the input beams pass through the constant deviation prisms (#1) in each input path. Each beam is deviated slightly (about 260 arcseconds) in different directions. The constant deviation prism is a compensated doublet so that light at different wavelengths has the same deviation. The outer annuli of the input beams are combined at the beam splitter. Part of the combined beam is diverted by the beam splitter onto the parabola which focuses the light to form two guiding spots on the CCD camera. Each guiding spot is intended to be positioned on a corner of four pixels. This enables the CCD to function as a quad cell. The guiding spot locations are used to correct the beam tilt of each input beam and maintain the parallelism of their wavefronts. The other part of the combined beam is diverted to the lower mirror, then reflected through the defocusing lens. Two annular shear spots (defocused) are formed by the parabola on the camera. The shear spots are employed to sense the beam walk of the input beams. A heterodyne metrology beam launcher is attached to the BC to measure the relative changes of the OPD of the input beams. The light source for the metrology beam is an IR laser at 1.3- $\mu\text{m}$  wavelength. The tip-tilt PZT controlled metrology mirror is used to align the metrology beam.

The assembled BC is shown in Figure 3. All optical components were mounted in a rigid light weight housing. This housing is designed to maintain optical alignments through launch. All optical components can be adjusted without disassembling the housing<sup>[1]</sup>.



(a) Front view

(b) Back view

Figure 3. Assembled beam combiner

### 3. FRINGE ANALYSES

#### 3.1 Least square fit (LSF) analyses of the dispersed fringes.

The intensity of the fringe image with the OPD shift,  $x(j)$ , at pixel  $i$  on the CCD camera can be written as

$$I(i, j) = I_1(i) + I_2(i) + 2\sqrt{I_1(i)I_2(i)} \cos(k(i)x(j) + \varphi_0)$$

where  $I_1(i)$  and  $I_2(i)$  are the two beam intensities on pixel  $i$ , respectively,  $k(i) = 2\pi/\lambda(i)$ ,  $\lambda$  is the wavelength at pixel  $i$ . For convenience we write the fringe intensity as

$$I(i, j) = a(i) + b(i)\sin(k(i)x(j)) + c(i)\cos(k(i)x(j))$$

where

$$a(i) = I_1(i) + I_2(i), \quad b(i) = -2\sqrt{I_1(i)I_2(i)} \sin\varphi_0, \quad c(i) = 2\sqrt{I_1(i)I_2(i)} \cos\varphi_0$$

The fringe intensity changes when the OPD shift in the delay line changes. Hence, a set of  $N$  fringe images can be taken with  $N$  different OPD shifts. The LSF algorithm is used to fit the set of the fringe images at each pixel. To produce the LSF curve, three parameters,  $a$ ,  $b$  and  $c$ , in the equation above must be determined. This is easily done as  $N > 3$ .

The flow chart in Figure 4 shows the LSF fringe processing. In our experiments a set of 50 fringe images are taken for the fringe analyses. The intensities of these 50 fringe images are fitted to a sine wave function at each pixel by assuming uniform OPD shift steps. The intensity difference,  $\Delta I$ , between the measured fringe intensity,  $I_{\text{exp}}$ , and the LSF curve,  $I_{\text{LSF}}$ , is calculated at each sample point. The OPD shift error between the measured and assumed OPD shift step is obtained by dividing the intensity difference by the slope of the LSF curve. Ideally for a given image each pixel should have the same OPD shift, however, the shift can be different due to the electronic effect on the CCD and wavelength calibration error. The OPD shift errors are averaged on each image to obtain the average OPD shift error,  $\Delta x_{\text{average}}$ . The OPD shift at each pixel is modified with  $\Delta x_{\text{average}}$  if the maximum absolute value of  $\Delta x_{\text{average}}$  of all images is larger than the required limit, which is 0.4 nm in our experiments. Then the intensities of the images are fitted to another sine function using the modified OPD shifts. The LSF processing loop will end until the maximum absolute value of  $\Delta x_{\text{average}}$  is less than the limit. Hence, a best-fit sine function to the image intensities is produced at each pixel. The fringes are characterized for the measured OPD shifts, fringe initial phase and visibilities.

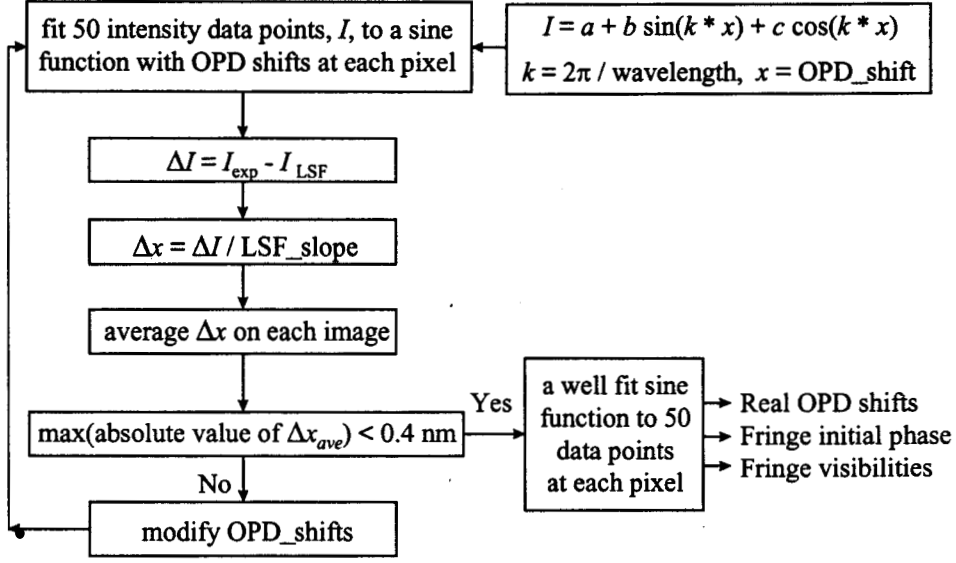


Figure 4. Fringe least square fit algorithm.

### 3.2 Fringe initial phase and visibility measurements.

After running the LSF algorithm, the OPD shift between two sampling positions is measured, and there is a LSF curve at each pixel. The initial phase raw (unwrapped) data and fringe visibility are derived as follows.

$$I = a + b \sin(k * OPD) + c \cos(k * OPD)$$

$$\Rightarrow I = a + amp * \cos(k * OPD + \phi_0)$$

$$\tan \phi_0 = -\frac{b}{c}, \quad amp = \sqrt{b^2 + c^2}$$

$$visibility \ \gamma = \frac{\sqrt{b^2 + c^2}}{a}$$

$$Normalized \ visibility \ \gamma' = \gamma * \frac{I_1 + I_2}{2\sqrt{I_1 I_2}}$$

where  $\phi_0$  is the raw data of the fringe initial phase,  $\gamma$  is the visibility,  $\gamma'$  is the normalized visibility, and  $I_1$  and  $I_2$  are the two input beam intensities at each pixel and measured by blocking each input beam in turn. The raw data of the initial phase over the selected wavelength range are unwrapped. The LSF algorithm is used to fit the unwrapped initial phases, then the initial OPD or phase is obtained.

$$unwrapped\_phase = const + OPD_0 \frac{2\pi}{\lambda}$$

where *const* is a constant, and  $OPD_0$  is the initial OPD of the two input beams.

## 4. Experimental results

### 4.1 Image recorded on the CCD camera.

A typical image recorded on the CCD camera is shown in Figure 5. A Mag light is used in the artificial star. The white light fringes are located on the bottom of the image. Two wavelengths (850 and 450 nm) bound the useable portion of the Mag light spectrum. The figure also shows that the fringe intensity increases as the wavelength increases. Hence, the signal to noise ratio of the fringes is relative low at short wavelength. The Mag light does not produce much light above the wavelength of 850 nm and below the wavelength of 450 nm.

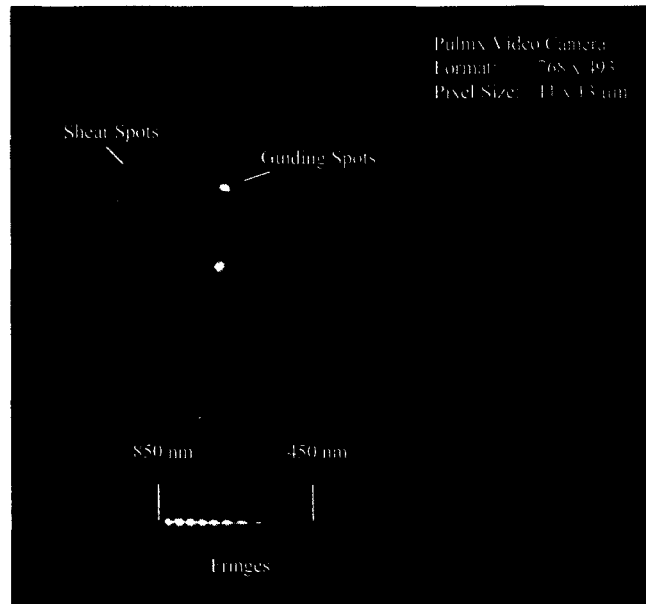


Figure 5. Beam combiner image on the CCD camera.

The 50 white light fringe images were recorded with a 40-nm shift step size in the OPD delay line. The set of 50 images is shown in Figure 6. The figure shows the white light fringe movement with the OPD shifts during the sampling.

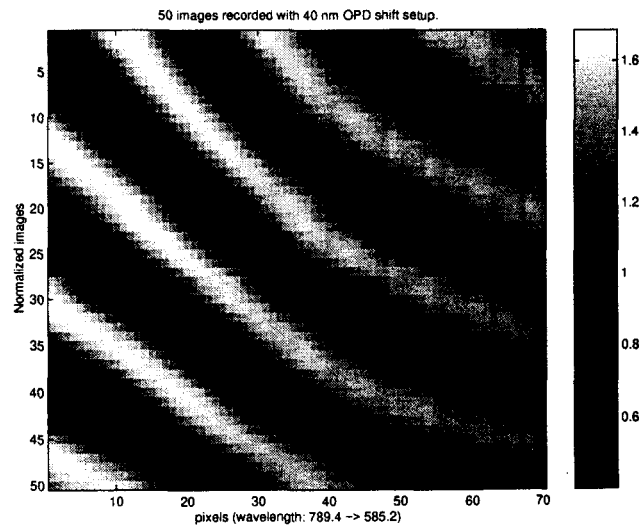


Figure 6. A set of 50 white light images.

#### 4.2 Fringe characteristics analyzed using the LSF algorithm.

The fringes were processed using the LSF algorithm discussed in section 3. A sine function was produced to fit these 50 data points at each pixel. The LSF loop started until the maximum absolute value of  $\Delta x_{\text{average}}$  was less than the limit. The experimental OPD shifts and fringe characterization were then determined.

The maximum absolute value of  $\Delta x_{\text{average}}$  as a function of LSF loop number is shown in Figure 7. The maximum value dropped fast from 130 nm to 1 nm in the first 6 LSF loops, then slowly reached the limit of 0.4 nm. This demonstrates that the LSF algorithm worked well and the maximum value of  $\Delta x_{\text{average}}$  approached a limit. The limit is determined by the measurement precision of the OPD shifts in the beam combiner under ordinary experimental conditions.

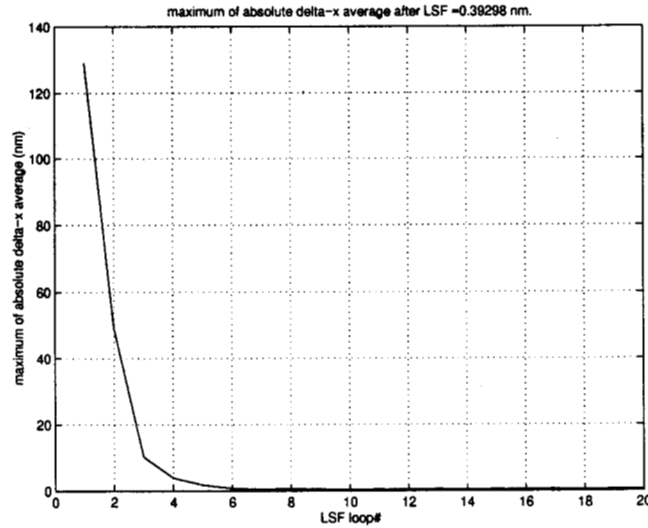


Figure 7. Maximum absolute value of  $\Delta x_{\text{average}}$  derived from the LSF algorithm.

The comparison of the experimental fringe intensity and LSF sine curves at 789-nm wavelength is shown in Figure 8. The solid line is the experimental fringe intensity curve as a function of sample point or OPD shift. The dash dot line is the LSF curve. These two curves show good agreement.

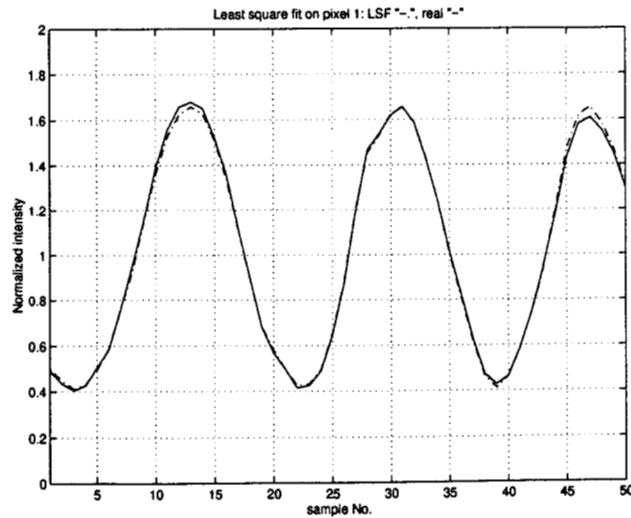


Figure 8. Comparison of the LSF and experimental fringe intensity curves.

The experimental OPD shift steps determined from the analyses of the test data are shown in Figure 9. The OPD shift step size was designed to be 40 nm, but this value was less than the average of the experimental OPD shifts, which is 44.5 nm. This means that the experimental average displacement rate of the PZT was 44.5 nm per volt instead of 40 nm per volt listed in the PZT specifications. The random deviations of the OPD shifts were caused by the PZT translation precision, air turbulence, and mechanical vibrations.

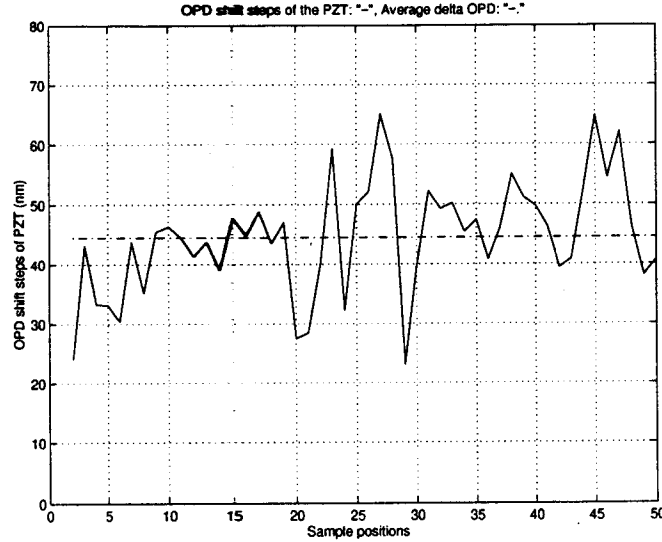


Figure 9. Optical shift measurements.

The raw data of the fringe initial phase as a function of wavelength are shown in Figure 10(a). It is necessary to unwrap the raw phase data since they had some discontinuities at certain wavelengths. The unwrapped phase curve is shown figure 10(b). The LSF algorithm discussed in section 3 was employed to process the unwrapped phase for the initial OPD of the two input beams. The initial OPD obtained was -6720.15 nm. The minus sign means that the optical path length of the lower input beam was longer than that of the upper input beam. Since the PZT movement decreased the path length of the lower input beam during the sampling, the fringes displayed on the CCD were moved toward the fringe central position where the fringes had the zero order. The total OPD change by the PZT was 2000 nm, less than the initial OPD. Therefore, none of the 50 images taken passed through the fringe center position.

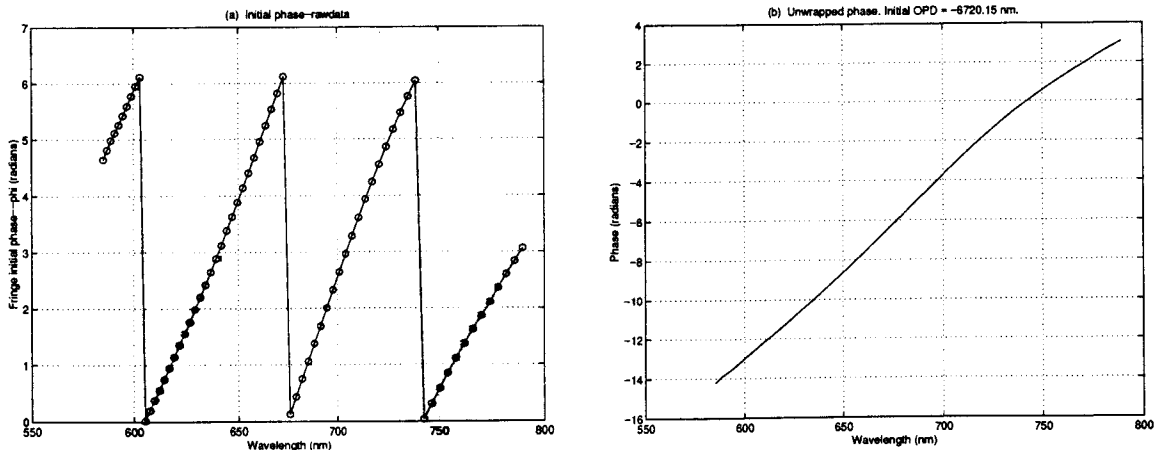
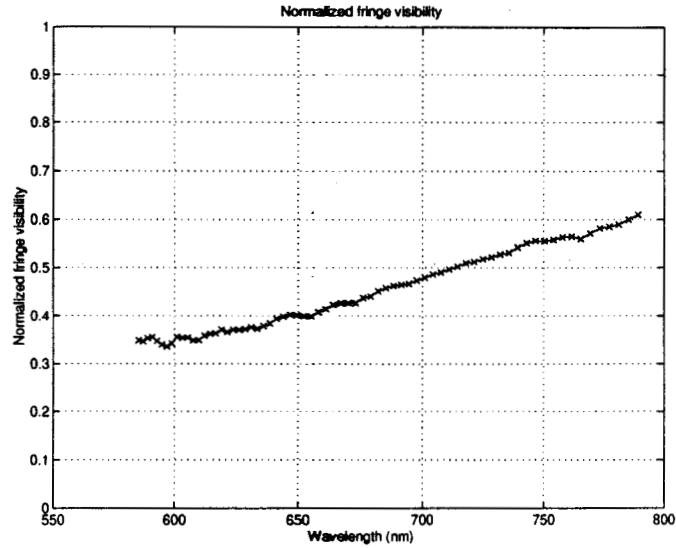


Figure 10. Fringe initial phase measurement.



The measured fringe visibilities are shown in Figure 11. The visibility varied from 0.33 to 0.61 over the selected wavelength range [585.2 nm, 789.4 nm]. The fringe visibility increases when the wavelength increases. The fringe contrast is greater at the longer wavelengths is clearly shown in Figure 5. The visibility variations via wavelength was caused by the wavefront errors via wavelength, which were due to the imperfect optical characteristics from each component used in the beam combiner and artificial star. The visibilities were also affected by the low signal to noise ratio on the short wavelength side of the fringes.



**Figure 11.** Fringe visibility measurement.

A comparison of the requirements for the space interferometer mission (SIM), the requirements for the BC design, and the measured performance of the BC function are listed in table 1. The table shows that the BC met all design requirements except for fringe visibility. The decreased fringe visibility performance is still under investigation.

**Table 1** Comparison of the requirements and performance of the BC.

Function	SIM	BC Design	BC measured
Static fringe visibility (combiner only)	0.85	0.85	0.33 - 0.61
Guiding spot throughput (including geometry)	0.14	0.14	0.16
Fringe throughput (including geometry)	0.20	0.20	0.24
Spectral resolution	6 nm	6 nm	2.3 nm/pixel
Fringe dispersion linearity	< 1%	< 5%	< 5% (550 - 800 nm) > 5% (800 nm)
Optical path tuning ranges ( $\mu\text{m}$ )	$\pm 18$	$\pm 18$	$\pm 21$
Beam splitter T/R (0.5 - 0.9 $\mu\text{m}$ )	< 60/40	< 60/40	< 60/40 (visible) 70/30 (1.3 $\mu\text{m}$ )

## 5. CONCLUSIONS

The BC has been designed, assembled and tested. The BC operates in white light and produces dispersed fringes for determining the OPD of the interfering beams, guiding spots for controlling beam wavefront tilt, and shear spots for controlling beam centration. The LSF algorithm described is effective in characterizing white light dispersed fringes. The OPD between the interfering beams can be varied by translating the fold mirror with the PZT. Scanning the OPD allows one to record fringe visibility as a function of wavelength. The fringe visibilities will be improved by using a light source which produces approximately uniform light intensity in the wavelength range of interest.

## ACKNOWLEDGEMENTS

This research was carried out at the Jet Propulsion Laboratory, California Institute of Technology, under a contract with the National Aeronautics and Space Administration. The authors would like to thank Don Moore, Gary Blackwood, and Yekta Gursel for useful discussion and assistance.

## REFERENCES

- [1] S. Shaklan, Y. Lin, R. Bartos, D. Moore and G. Blackwood, Beam combiner brassboard hardware document, *Space Interferometer Mission*, Jet Propulsion Laboratory, August, 1997.
- [2] Y. Lin, R. Bartos, S. Shaklan and G. Blackwood, Beam combiner test document, *Space Interferometer Mission*, Jet Propulsion Laboratory, August, 1997.
- [3] R. P. Korechhoff, S. Shaklan, Y. Lin, R.D. Bartos and D. M. Moore, "Design and performance of an astrometric beam combiner for space interferometry", *SPIE*, Vol. 3350, March 20-28, 1998.
- [4] K. Creath, Phase-measurement interferometry techniques, *Progress in Optics*, XXVI, 1988, pp. 350-393.